Design of the Deformable Mirror Demonstration CubeSat (DeMi)

Ewan S. Douglas^a, Joseph S. Figura^a, Christian A. Haughwout^a, Jennifer N. Gubner^a,b, Alex A. Knoedler^a, Sarah LeClair^a,c, Thomas J Murphy^a, Nikolaos Skouloudis^a, John Merk^d, Roedolph A. Opperman^a,d, and Kerri L. Cahoy^a,e

^aDepartment of Aeronautics and Astronautics, Massachusetts Institute of Technology, Cambridge, MA, USA.
^bDepartment of Physics, Wellesley College, Wellesley, MA, USA.
^cSouth Kingstown High School, Wakefield, RI, USA.
^dAurora Flight Sciences, Cambridge, MA, USA.
^eDepartment of Earth, Atmospheric and Planetary Sciences, Massachusetts Institute of Technology, Cambridge, MA, USA.

ABSTRACT

The Deformable Mirror Demonstration Mission (DeMi) was recently selected by DARPA o demonstrate in-space operation of a wavefront sensor and Microelectromechanical system (MEMS) deformable mirror (DM) payload on a 6U CubeSat. Space telescopes designed to make high-contrast observations using internal coronagraphs for direct characterization of exoplanets require the use of high-actuator density deformable mirrors. Space telescopes designed to make high-contrast observations using internal coronagraphs for direct characterization of exoplanets require the use of high-actuator density deformable mirrors. These DMs can correct image plane aberrations and speckles caused by imperfections, thermal distortions, and diffraction in the telescope and optics that would otherwise corrupt the wavefront and leaking allow starlight to contaminate coronagraphic images. DeMi wiill provide term on-orbit demonstration and performance characterization of a MEMS deformable mirror and closed loop wavefront sensing.

The DeMi mission has two operational modes, one mode that images an internal light source and another mode which uses an external aperture to images stars. Both the internal and external modes include image plane and pupil plane wavefront sensing. The objective of the internal measurement of the 140-actuator MEMS DM actuator displacement is to characterizing the mirror performance and demonstrate closed-loop correction of aberrations in the optical path. Using the external aperture to observe stars of magnitude 2 or brighter, and assuming 3-axis stability with less than 0.1 degree of attitude knowledge and jitter below 10 arcsec RMSE, per observation, DeMi will also demonstrate closed loop wavefront control on an astrophysical target. We present an updated payload design, results from simulations and laboratory optical prototyping, as well as present our design for accommodating high-voltage multichannel drive electronics for the DM on a CubeSat.

Keywords: deformable mirrors, MEMS, wavefront sensing, high-contrast imaging, exoplanets, transits.

1. INTRODUCTION

Microelectromechanical deformable mirror technology[1] has found a variety of uses, from adaptive optics for correction of atmospheric turbulence,[2] and in-vivo imaging of the human retina,[3] to a design for a wide-field scanning telescope[4] and maximizing the contrast of a nulling interferometer for exoplanet imaging.[5] Deformable Mirror (DM)s are a critical technology for planned internal space coronagraphs to directly image extrasolar planets.[6] A single DM can correct phase and amplitude errors across half of a coronagraphic image[7] and two
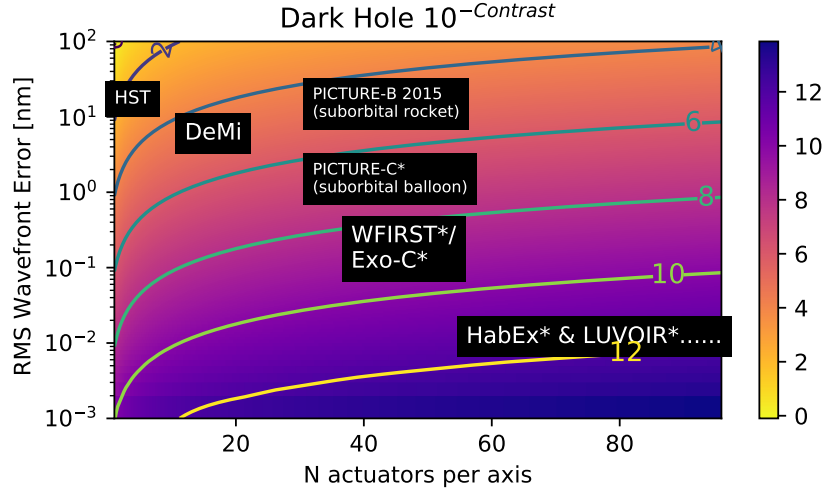

Figure 1: Heatmap of dark-hole contrast with axes showing wavefront error versus the number of actuators across the mirror aperture at 633 nm. (The DeMi payload does not include a coronagraph).

in series allow simultaneous correction of both phase and amplitude terms across a "dark hole" symmetrically around the stellar Point Spread Function (PSF).[8]

Neglecting amplitude errors, a simple derivation of dark hole contrast (C) as a function of controlled root mean squared (RMS) wavefront error (h_{RMS}) and the number of DM actuators across the pupil (N), or the number of spatial modes corrected, is given by Traub and Oppenheimer [9, equation 124]:

$$C = \pi \left(\frac{4h_{rms}}{N\lambda} \right) \tag{1}$$

The approximate performance of several missions on this curve is shown in Fig. 1, including two suborbital missions: the PICTURE[10] sounding rocket flights of 2011 and 2015, which tested a 32x32 actuator microelectromechanical systems (MEMS) DM and the PICTURE-C balloon.[11] Mission designs for imaging hot Jupiters and exozodiacal dust call for two 48×48 DMs, such as the Wide-Field InfrarRed Survey Telescope (WFIRST) Coronagraph Instrument (CGI).[12] The Exo-C design similarly called for $\geq$ 48 actuators across the telescope aperture.[13] Further in the future, proposed missions such as Habitable Exoplanet Imaging Mission (HabEx) and Large UV/Optical/Infrared Surveyor (LUVOIR) call for as many as 195 actuators across the telescope aperture.[14]

Deformable mirrors in space hold promise beyond exoplanet imaging; other applications include laser communications,[15, 16] reconfigurable optical assemblies,[17] or deployable apertures.[18] The DeMi payload will haracterize the performance of a MEMS deformable mirror in low earth orbit, decreasing the technological risk to future applications.

A 6U CubeSat bus[19] provides sufficient power and volume for the relatively straightforward implementation of wavefront sensing and control. A Blue Canyon Technologies XB6 spacecraft bus has been selected to host the DeMi payload. The XB6 bus includes an XACT attitude determination and control system for sub-10 arcsecond pointing stability (1σ).[20] The following sections of this proceeding will focus on the optical and electrical design of the DeMi payload and a brief discussion of to possible astrophysical targets.

2. OPTICAL DESIGN

The primary objective of the DeMi mission is detailed characterization of MEMS DM operation in space. In addition, the payload is designed to perform active wavefront correction in space, observe and correct stellar PSFs, and test wavefront retrieval and control algorithms.

The key component of the DeMi payload is the DM. A 140-actuator, continuous phase-sheet Boston Micro-machines (Cambridge, MA, USA) Multi-DM has been selected for its compact form factor and large stroke (1.5 to 5.5 microns surface displacement).

Both a Michelson interferometer and a Shack-Hartmann wavefront sensor[21] were considered for DM characterization in early DeMi designs.[22, 23] As the DeMi design has evolved, a Shack-Hartmann sensor has been selected as it allows measurement of wavefront errors of several microns without moving parts.[24–26]

Fig. 2a shows a top view of the payload ray trace. For astronomical observations, a telescope is formed by a 50 mm, f/4 off-axis parabola (OAP) primary mirror, which is focused on a field mirror, and a 12.7 mm, f/1.2 OAP which collimates the beam onto the DM. A single-mode optical fiber, embedded in the field mirror and fed by a laser diode, approximates a point source for internal calibration experiments. A 12.7mm, f/1.2 OAP collimates the beam onto the DM. After the DM the corrected wavefront is split between an imaging camera and a pupil relay, which feeds the Shack-Hartmann Wavefront Sensor (SHWFS). A computer-aided-design rendering of the current payload design is shown in Fig. 4.

The telescope mirrors and optical bench are manufactured from aluminum, providing coefficient of thermal expansion (CTE) matching to minimize telescope thermal sensitivity. The eye-safe (less tham 5mW), approximately 635 nm internal laser diode provides an alternative light source, decreasing risks and allowing measurements of the mirror surface without pointing requirements and with minimal photon noise.

Table 1: Design optoelectrical properties. The effective quantum efficiency includes both detector sensitivity and optical losses. The nominal lenslet array is a Thorlabs MLA150M-5C.

Term	Value
Primary Aperture, A	30 mm
Throughput and QE	0.2
Effective bandwidth	150 nm
CMOS detectors	MT9P031, Pixelink PL-D775MU-BL
Gain G	1
Dark Noise Rate,[27] D	16 e$^-$/sec
Digitization noise, DN	1/12
Read noise,[28] RN	2.4 e$^-$
Pixel Size	2.2 μm
Telescope magnification	7
Lenslet Pitch	150 μm
Effective Lenslet Focal Length	3.7 mm

2.1 Wavefront Sensing Budget

In order to characterize a MEMS deformable mirror across it's full stroke, a wavefront sensor (WFS) with large dynamic range is required. The classic SHWFS is limited at large wavefront tilts by confusion between spots outside the area of their respective lenslet and at small displacements by centroiding error. The former limit can be set by the lenslet pitch and focal length. The latter limit requires accurate modeling of centroid error. In order to characterize the sensitivity of the DeMi SHWFS, we develop semi-analytic and numerical models of centroid error.

Centroid error arising from time dependent random processes, such as photon noise and detector noise, are estimated by propagation of uncertainty through a simple centroid model.[29] We first estimate the two-dimensional Airy function $\alpha(x, y)$ in units of electrons per second as a function of stellar magnitude using the POPPY[30] "misc.airy_2d" function and astropy units.[31] The total variance per pixel in the detector (x, y) plane for time t is given by [29, Eq. 4.7]:

$$\sigma^2(x, y, t) = RN^2 + D \times t + \alpha(x, y) \times t + DN \tag{2}$$

and the centroid error in the x-axis is given by [29, Eq. 4.9]:

$$\sigma^2_{<x>} = \frac{\sum_i^N \sigma^2 dx^2}{\sum_i^N \sigma^2} \tag{3}$$

where dx is the distance between each pixel and the centroid, $< x >$. The mean centroid error versus V-band magnitude in both axes is shown in Fig. 3a for several temporal sampling rates. 24×24 lenslet and 36×36 pupil sampling levels are also shown, illustrating the trade between wavefront precision and spatial resolution in this photon limited regime.

The impact of quantum efficiency (QE) (or photo response non-uniformity (PRNU)) variation on centroiding will initially be corrected before launch via flat-field correction, but on-orbit radiation will alter pixel responsivities. The impact on our detector was estimated numerically, first by measuring centroid of a PSF[30] without PRNU then applying quantum efficiency variations with increasing variation by increasing the standard deviation of a pixel sensitivity array with a mean of unity and a Gaussian distribution. Fig. 3b shows the centroid error (left axis) and wavefront tilt error (right axis) versus increasing quantum efficiency. From left to right, dashed vertical lines show the un-irradiated, 0.5 krad(Si), 1 krad(Si), and 5 krad(Si) pixel-to-pixel variation for the chosen MT9P031 complementary metal-oxide-semiconductor (CMOS) detector.[27] The centroid error is independent of incident flux and will impact both laser and stellar observations. Thus, for the typical low-earth-orbit CubeSat radiation dose (< 1 krad/year),[32] the centroiding error will place a limit on the SHWFS sensitivity to wavefront tilt per lenslet of 1 nm or lower.

2.2 Photometric Sensitivity

Despite a small aperture, as a telescope in space, the DeMi telescope provides a platform recording precision photometric light curves of bright stars. A preliminary analysis using the parameters in Table 1 and neglecting PRNU variation predicts photometric sensitivity per orbit, at SNR=5, to one part in 3000 (a Neptune-like transit depth) around a Sunlike star brighter than V-mag of approximately 2.5.

2.3 Prototype Layout

To understand and estimate the expected payload performance, we have begun component level testing and construction of a benchtop prototype. The most recent testing was done on the layout shown in Figure 2b. The primary goal was to observe the operation of a deformable mirror and test the performance of the CMOS cameras and a commercial SHWFS.

With a refracting telescope providing collimated beam, main components in the optical setup are the laser, the large and small OAP, the DM, the beam splitter, the camera, and the wavefront sensor. While the present payload design calls for a CMOS detector behind the SHWFS, initial testing of a 150 μm lenslet array was performed with a commercial CCD based SHWFS sensor (Thorlabs WFS150-5C). From initial testing of the WFS, the lowest achievable standard deviation measurement in the wavefront was approximately 0.02 μm.

The WFS was also used to test the operation of the DM. We were able to observe the actuation of all points in the array and take measurements on the adjusted wavefront. The results of one of these tests are shown in Figure 5.

3. ELECTRICAL DESIGN

The DeMi payload electrical system is responsible for reading out imaging and wavefront sensing cameras, controlling the deformable mirror, monitoring DM operation, and relaying data to the spacecraft bus. The design includes two cameras, two processors, two industrial grade SD cards for storage, the DM driver, a calibration laser and driver, and a heater. Note that spacecraft electrical functions including communication, attitude control, power generation, and others are handled by the XB6 bus. The electrical system and its interfaces to the optical system and XB6 bus are shown in the block diagram in Figure 6.
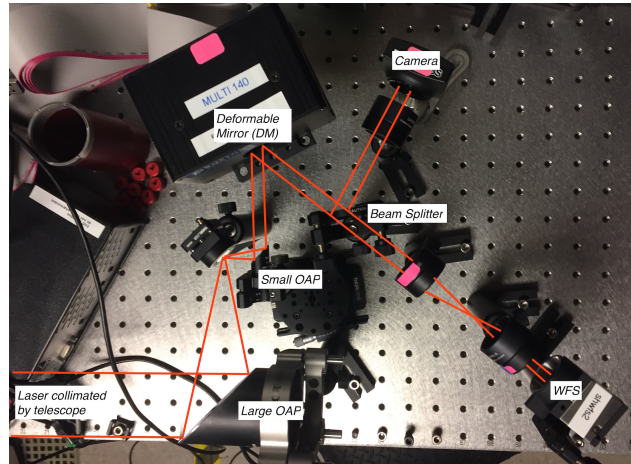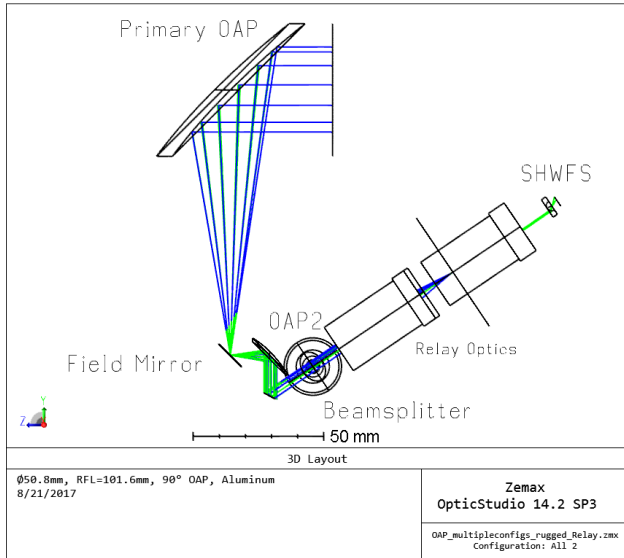
(a) Ray trace of the current payload optical design. Counter-clockwise from top right: a 50mm OAP, a flat field mirror for fiber injection, a 12.7mm collimating OAP, the deformable mirror, a beamsplitter sending light to the imaging camera and a pupil relay and SHWFS.

(b) The laboratory optical setup used to prototype and test the integration of the optical components, cameras, and sensors.

Figure 2: Optical layouts.
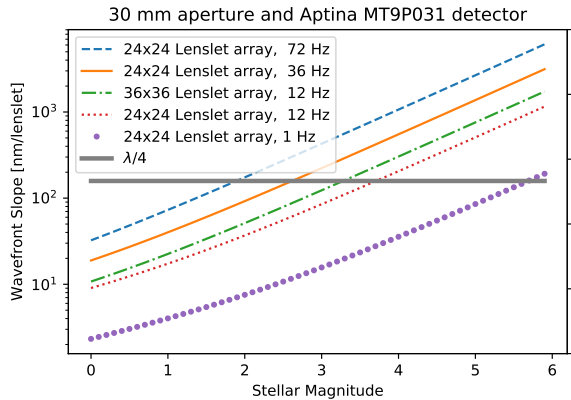
(a) Predicted wavefront error versus V-band magnitude for different exposure times and lenslet sampling intervals.
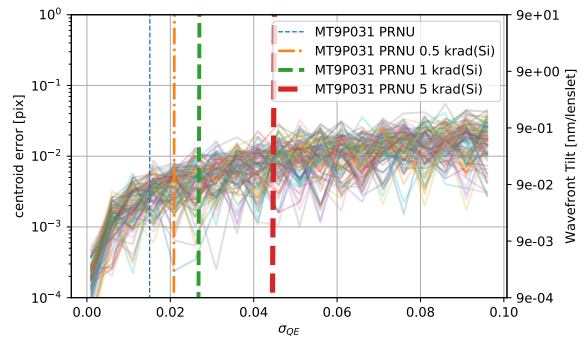
(b) 100 curves of centroiding error (left axis) or wavefront tilt (right axis) versus the standard deviation of pixel quantum efficiency (σ_{QE}) for randomly generated sensitivity maps. Each iteration includes 20 independent maps of increasing σ_{QE}.

Figure 3: Wavefront sensitivity curves.

3.1 Command, Data Handling, and Communication

The payload computer is responsible for commanding the payload and processing the outputs of the two cameras. The selected flight computer is the Raspberry Pi Compute 3 module, a low cost and lightweight microprocessor produced by the Raspberry Pi Foundation. The Raspberry Pi runs Linux and has built-in SPI, USB and GPIO interfaces, providing all of the processing functionality necessary for the DeMi Payload.[?] The Pi is also planned for use as the flight computer on STRaND-2, a 3U CubeSat developed by the University of Surrey, and on
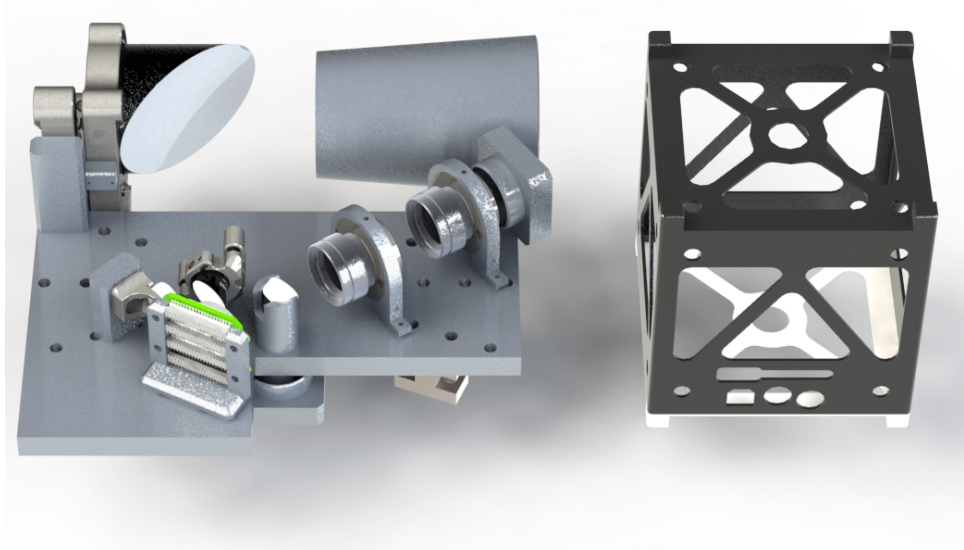
Figure 4: Prototype payload optomechanical layout. Rendering of the preliminary payload mechanical layout (Credit A. Knoedler). Light enters horizontally from the top right through the conical baffle. The optical bench and telescope OAP mirrors will be fabricated from aluminum to minimize CTE mismatches. A 1U Cubesat structure (100 mm on a side) is shown at right for scale.
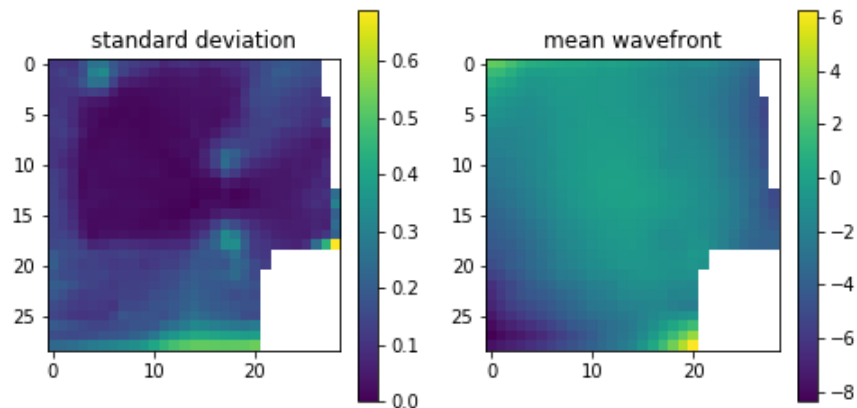

Figure 5: The resulting wavefront and standard deviation calculation taken from the wavefront sensor of the actuation of 3 different actuators on the DM. Two opposite corner actuators and one actuator in the middle of one of the sides

AArest, a multi-CubeSat mission developed jointly by Caltech and the University of Surrey.[?] Collected data and the Raspberry Pi's operating system will be stored on two industrial grade SD cards. Two Raspberry Pis and two SD cards will be flown to provide redundancy against a hardware failure. The two Raspberry Pi modules, SD cards, and supporting electronics will be mounted on a custom board.

The payload computer has four data interfaces: the two imagers are connected to the computer via USB, the DM driver is commanded with SPI, and the heater and calibration laser are controlled with GPIO interfaces to their respective drivers. Communication between the payload computer and the XB6 bus will be provided by a UART serial interface.
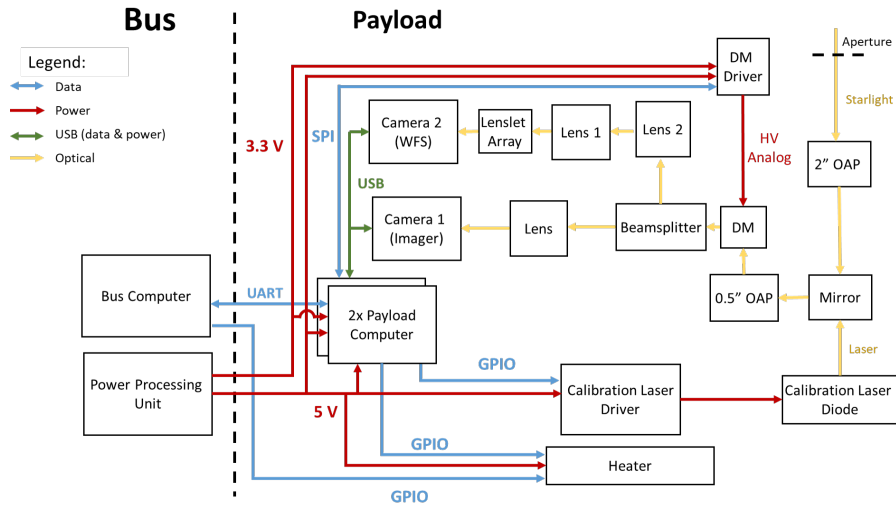
Figure 6: A block diagram of the DeMi electrical system optical system. (Credit J. Figura)

The XB6 bus will use two radios to communicate with the ground. The Cadet[33] is a software defined UHF radio supplied by L3-Communications out of Salt Lake City, UT. The Cadet can achieve 3 Mb/s downlink rate when communicating with Wallop Island's UHF ground station. It is intended as the primary radio for science data. The Lithium-1 radio[34] is produced by Astronautical Development (AstroDev), headquartered in Ann Arbor, MI. Lithium-1 operates at a data rate of 9.6 kb/s and will primarily be used for command, control and telemetry of the spacecraft.

During regular operations, frames from the camera are passed to the flight computer and processed to produce the relevant data products. These data products are stored on the SD cards until being passed to the bus to be downlinked. A data budget is shown in Table 2. Three example data products are identified: the region of interest on the imager, the state of each actuator in the deformable mirror, and the centroids of the wavefront sensor. An example observation of five minutes of sampling at 12 frames per second is shown, and the storage margin is calculated for an 8 GB SD card with 2 GB reserved for the Pi's operating system. The number of passes to downlink this observation is calculated using the Lithium or Cadet radios. The data budget shows that five minutes of observations take only 2.6% of the available storage, and can be downlinked in less than a second with the cadet.

Table 2: Projected DeMi Data Budget, showing data products and an example observation.

Observation Data Produced				
Data Product	Dimensions	Total Values	Bits	Total Bits (Mb)
Imager ROI	128 x 128	16384	12	0.197
DM Values	12 x 12	144	14	0.002
WFS Centroid	48 x 48	2304	64	0.147
		Total Data per Sample:		0.346

Example Observation	
Duration	5 min
Data / Sample	0.346 Mb
Sample Rate	12
Total Data Stored:	1246 Mb
Total Storage	48000 Mb
Storage Remaining	46754 Mb

Downlinking Example Observation		
Data Stored	1245.6 Mb	
Averaging	Every 10 frames	
Compression Factor	0.7	
Data to Downlink	87.192 Mb	
Downlink Radio:	Lithium	Cadet
Data Rate (Mb/s)	0.0096	3
Pass Duration (min)	10	10
Passes to Downlink		
Example Observation	15.1	0.05

3.2 DM Driver

To actuate the DM, each channel must be supplied a variable voltage that can be as high as 250V. A hardware driver must be used to generate these voltages. The existing Boston Micromachines driver for the Multi-DM is 7 inches by 7 inches by 2.5 inches, far too large to fit in a CubeSat.[?] Consequently, MIT is developing a miniaturized driver which repackages the Boston Micromachines driver architecture into a CubeSat form-factor. This size reduction is achieved by foregoing the Boston Micromachines driver's large user-friendly connectors and cooling fans, as well as implementing high density circuit routing on the printed circuit boards. Additionally, the MIT driver differs from the Boston Micromachines driver by the addition of a separate current monitor for each set of 32 high voltage outputs.

The driver consists of a high-voltage power supply and six pairs of digital-to-analog converters (DAC) and amplifiers. The high-voltage power supply steps up the voltages provided by the bus, and supplies that power to the amplifier. Each analog-to-digital converter is commanded by the payload computer over an SPI interface. Outputs of the DAC are fed into a high voltage amplifier, producing the desired output voltage. Each DAC and amplifier unit has 32 channels, and six pairs are used to control all 140 DM channels (52 channels are not used). It would suffice to have 5 DAC/amplifier pairs for a total of 160 channels; however, to decrease development time and risk, two identical boards with three DAC/amplifier pairs on each are used, rather than one board with three DAC/amplifier pairs and another board with only two.
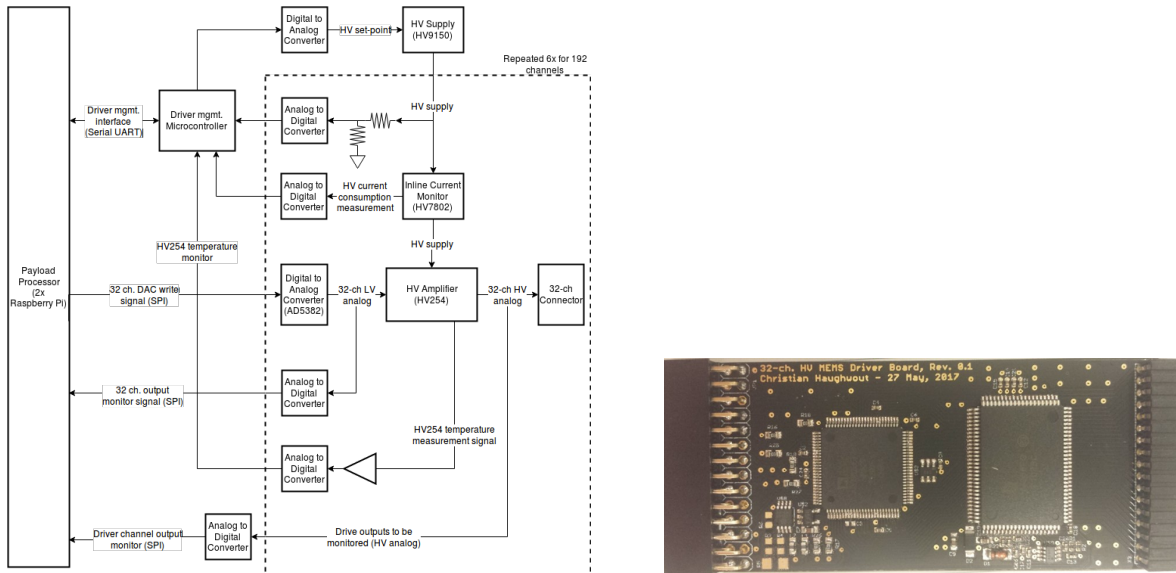

Figure 7: The DeMi DM Driver. Left, a block diagram of the board design. Right, one populated unit consisting of an ADC and amplifier. (Credit C. Haughwout)

3.3 Power

The bus handles power generation and storage, and provides 3.3 V and 5 V rails to the payload. Additional power processing for the calibration laser and the DM is handled by the laser driver and DM driver, respectively.

A preliminary power budget, shown in Table 3, predicts that the payload will consume 18.1 Watts of power while operating. The budget shows the power consumption of each electrical component in each operational mode. Gray squares indicate that the component is off, yellow squares that the component is idle, and green squares that the component is operating nominally. The power consumption of the two cameras and the calibration laser is based on manufacturer specifications. Raspberry Pi numbers are based on estimates for the Pi with some functionality disabled. The DM driver's power usage is estimated based on the power consumption of driver developed by NASA Ames for the larger BMC Kilo DM. The Ames driver controlled a 1024 channel DM, compared to DeMi's 140 channel DM, and consumed 6.6 Watts during operation.[35] This power number is used

as a conservative estimate for MIT's DM driver. The heater is assumed to consume 5 Watts at all times, which may be revised downwards pending further thermal analysis. As development of the payload continues, the power budget will be updated with experimentally collected numbers.

Table 3: Projected DeMi power budget for four operating modes.

Component	Payload Off (W)	Safe Mode (W)	Standby (W)	Internal Observation (W)	External Observation (W)
Camera 1 (Imager)	0	0	2	2	2
Camera 2 (WFS)	0	0	2	2	2
DM Controller	0	1.5	1.5	6.6	6.6
Payload Computer	0	2.5	2.5	2.5	2.5
Calibration Laser	0	0	0	0.02	0
Heater	0	5	5	5	5
Total Power	**0**	**9**	**13.5**	**18.52**	**18.5**

4. TARGET SELECTION

While the primary mission of the DeMi payload is DM characterization, the small aperture also affords some opportunities for space-based photometry.

In order to best view the stars, the stars must be extremely bright; at a low order of magnitude of light, the star provides a more easily detectable change in light during a transit. Additionally, it is logical to concentrate on main-sequence dwarfs with spectral types F5 to M5. Low mass dwarf stars are preferable due to their high abundance and facilitation of transiting planet detection. Evolved stars and early-type dwarfs are large, inhibiting the detection of small planets. Next, stars with high metallicity are more likely to host planets.[36]

Table 4 depicts the main target stars for the DeMi mission. These stars were selected based on their apparent magnitude, rather than their absolute magnitude, to improve the detectability and measurement of the stars. These target stars are all of different spectral types, some not within the ideal M to F spectral type, but are still optimal to view due to their low magnitude apparent brightness. Other target stars were found by use of the Exoplanet Catalog. The spectral criteria were used to narrow down the large quantity of stars to a sortable list, which was then divided by taking the brightest half of stars and the closer half of the star distance. This would ensure that the stars would have a higher apparent magnitude and correspond to the ideal spectral types. Based on these criteria, 433 total stars were found and sorted. The main target stars were then modeled on the STK program with an orbit based on the ISS orbit. In order to gain a broader understanding of the optimal conditions for the DeMi satellite, the orbit was altered with varying altitudes and angles. Considering general parameters for the orbit (400km - 600 km orbit and an inclination sufficient to fly over MIT), it is observed that the main target stars would be in view in coordination with the umbra.

Table 4: Five brightest stars as viewed from Earth and DeMi mission target stars.

Name	Apparent Magnitude	Absolute Magnitude	Distance (light years)	Spectral Type
Rigil Kentaurus	-0.27	4.4	4.37	G2V+K1V
Arcturus	-0.04	0.2	36.7	K1.5IIIp
Canopus	-0.72	-2.5	313	A9II
Sirius	-1.46	1.4	8.61	A1Vm
Vega	0.03	0.6	25.1	A0Va

5. FUTURE WORK

This work presents a snapshot of the work in progress on the DeMi CubeSat payload.

Moving forward, the optomechanical design will be developed to survive the launch and orbit environments.[37] Custom SHWFS retrieval algorithms will be implemented, along with a CMOS detector providing higher resolution sampling of the spotfield. The prototype DM driver board will be tested and the design will be extended to three DAC/amplifier pairs per board. The power budget will revised with measured component draws under realistic loads.

ACKNOWLEDGMENTS

REFERENCES

[1] Bifano, T. G., Perreault, J., Mali, R. K., and Horenstein, M. N., "Microelectromechanical deformable mirrors," *IEEE Journal of Selected Topics in Quantum Electronics* **5**, 83–89 (Jan. 1999).

[2] Morzinski, K. M., Evans, J. W., Severson, S., Macintosh, B., Dillon, D., Gavel, D., Max, C., and Palmer, D., "Characterizing the potential of MEMS deformable mirrors for astronomical adaptive optics," in [*Proc SPIE*], **6272**, 627221–627221–12 (2006).

[3] Doble, N., Yoon, G., Chen, L., Bierden, P., Singer, B., Olivier, S., and Williams, D. R., "Use of a micro-electromechanical mirror for adaptive optics in the human eye," *Optics letters* **27**(17), 1537–1539 (2002).

[4] Scott, C., Potsaid, B., and Wen, J. T., "Wide Field Scanning Telescope Using MEMS Deformable Mirrors," *International Journal of Optomechatronics* **4**, 285–305 (Aug. 2010).

[5] Rao, S. R., Wallace, J. K., Samuele, R., Chakrabarti, S., Cook, T., Hicks, B., Jung, P., Lane, B., Levine, B. M., Mendillo, C., Schmidtlin, E., Shao, M., and Stewart, J. B., "Path length control in a nulling coronagraph with a MEMS deformable mirror and a calibration interferometer," in [*Proc. SPIE*], **6888**, 68880B–68880B (Feb. 2008).

[6] Siegler, N., "Exoplanet Exploration Program Technology Plan Appendix: 2016," tech. rep., Jet Propulsion Laboratory (2016).

[7] Malbet, F., Yu, J. W., and Shao, M., "High-Dynamic-Range Imaging Using a Deformable Mirror for Space Coronography," *Publications of the Astronomical Society of the Pacific* **107**(710), 386–398 (1995).

[8] Pueyo, L., Kay, J., Kasdin, N. J., Groff, T., McElwain, M., Give'on, A., and Belikov, R., "Optimal dark hole generation via two deformable mirrors with stroke minimization," *Applied optics* **48**(32), 6296–6312 (2009).

[9] Traub, W. A. and Oppenheimer, B. R., "Direct imaging of exoplanets," in [*Exoplanets*], 111–156, University of Arizona Press, Tucson, AZ, USA (2010). Seager, S., ed.

[10] Douglas, E. S., Mendillo, C. B., Cook, T. A., and Chakrabarti, S., "Wavefront Sensing in Space from the PICTURE-B Sounding Rocket," *Proc. SPIE* **9904-252** (2016).

[11] Cook, T., Cahoy, K., Chakrabarti, S., Douglas, E., Finn, S. C., Kuchner, M., Lewis, N., Marinan, A., Martel, J., Mawet, D., Mazin, B., Meeker, S. R., Mendillo, C., Serabyn, G., Stuchlik, D., and Swain, M., "Planetary Imaging Concept Testbed Using a Recoverable ExperimentCoronagraph (PICTURE C)," *J. Astron. Telesc. Instrum. Syst* **1**(4), 044001–044001 (2015).

[12] Sidick, E., Seo, B.-J., Marx, D., Poberezhskiy, I., and Nemati, B., "WFIRST / AFTA coronagraph contrast performance sensitivity studies: simulation versus experiment," 99126M (July 2016).

[13] EXO-C STDT., Chair, K. S. and EXO-C Design Team., Lead., F. D., [*EXO-C Final Report- Imaging Nearby Worlds*], CL (2015).

[14] Morgan, R. and Siegler, N., "Initial look at the coronagraph technology gaps for direct imaging of exo-earths," in [*Proc. SPIE*], **9605**, 96052I (Sept. 2015).

[15] Bifano, T., Schatzberg, L., Stewart, J., and Cornelissen, S., "MEMS Modulated Retroreflectors for Secure Optical Communication," *ASME International Mechanical Engineering Congress and Exposition. Nano-Manufacturing Technology; and Micro and Nano Systems, Parts A and B* **Volume 13**, 395–399 (Jan. 2008).

[16] Stewart, J. B., Murphy, D. V., Moores, J. D., Fletcher, A. S., and Bonneau, K. M., "Comparing adaptive optics approaches for NASA LCRD Ground Station #2," 86100M (Mar. 2013).

[17] Underwood, C., Pellegrino, S., Lappas, V. J., Bridges, C. P., and Baker, J., "Using CubeSat/micro-satellite technology to demonstrate the Autonomous Assembly of a Reconfigurable Space Telescope (AAReST)," *Acta Astronautica* **114**, 112–122 (2015).

[18] Champagne, J., Hansen, S., Newswander, T., and Crowther, B., "CubeSat Image Resolution Capabilities with Deployable Optics and Current Imaging Technology," *AIAA/USU Conference on Small Satellites* (Aug. 2014).

[19] SLO, C. P., "6u CubeSat Design Specification Rev. PROVISIONAL," (Apr. 2016).

[20] Mason, J., Baumgart, M., Woods, T., Hegel, D., Rogler, B., Stafford, G., Solomon, S., and Chamberlin, P., "MinXSS CubeSat On-Orbit Performance and the First Flight of the Blue Canyon Technologies XACT 3-axis ADCS," *AIAA/USU Conference on Small Satellites* (Aug. 2016).

[21] Platt, B. C. and Shack, R., "History and Principles of Shack-Hartmann Wavefront Sensing," *J Refract Surg* **17**, S573–S577 (Sept. 2001).

[22] Cahoy, K. L., Marinan, A. D., Novak, B., Kerr, C., and Webber, M., "Wavefront control in space with MEMS deformable mirrors," in [*Proc SPIE*], **8617**, 861708–861708–16 (2013).

[23] Cahoy, K. L., Marinan, A. D., Novak, B., Kerr, C., Nguyen, T., Webber, M., Falkenburg, G., Barg, A., Berry, K., Carlton, A., Belikov, R., and Bendek, E. A., "MEMS deformable mirror CubeSat testbed," in [*Proc SPIE*], **8864**, 88640U–88640U–17 (2013).

[24] Marinan, A., Cahoy, K., Webber, M., Belikov, R., and Bendek, E., "Payload characterization for CubeSat demonstration of MEMS deformable mirrors," in [*Proc. SPIE*], **9148**, 91483Z–91483Z–16 (2014).

[25] Marinan, A., Cahoy, K., Merk, J., Belikov, R., and Bendek, E., "Improving Nanosatellite Imaging with Adaptive Optics," *AIAA/USU Conference on Small Satellites* (Aug. 2016).

[26] Marinan, A. D., *Improving nanosatellite capabilities for atmospheric sounding and characterization*, thesis, Massachusetts Institute of Technology (2016).

[27] Becker, H. N., Dolphin, M. D., Thorbourn, D. O., Alexander, J. W., and Salomon, P. M., [*Commercial sensory survey radiation testing progress report*], Pasadena, CA: Jet Propulsion Laboratory, National Aeronautics and Space Administration (2008).

[28] Enright, J., Doug Sinclair, and Christy Fernando, "COTS Detectors for Nanosatellite Star Trackers: A Case Study," DigitalCommons@USU, Utah State University (2011).

[29] Mendillo, C. B., *Scattering properties of dust in Orion and the Epsilon Eridani exoplanetary system*, PhD thesis, Boston University, Boston, MA, USA (2013).

[30] Perrin, M., Long, J., Douglas, E., Sivaramakrishnan, A., Slocum, C., and others, "POPPY: Physical Optics Propagation in PYthon," *Astrophysics Source Code Library* , ascl:1602.018 (Feb. 2016).

[31] The Astropy Collaboration, Robitaille, T. P., Tollerud, E. J., Greenfield, P., Droettboom, M., Bray, E., Aldcroft, T., Davis, M., Ginsburg, A., Price-Whelan, A. M., Kerzendorf, W. E., Conley, A., Crighton, N., Barbary, K., Muna, D., Ferguson, H., Grollier, F., Parikh, M. M., Nair, P. H., Gnther, H. M., Deil, C., Woillez, J., Conseil, S., Kramer, R., Turner, J. E. H., Singer, L., Fox, R., Weaver, B. A., Zabalza, V., Edwards, Z. I., Azalee Bostroem, K., Burke, D. J., Casey, A. R., Crawford, S. M., Dencheva, N., Ely, J., Jenness, T., Labrie, K., Lim, P. L., Pierfederici, F., Pontzen, A., Ptak, A., Refsdal, B., Servillat, M., and Streicher, O., "Astropy: A community Python package for astronomy," *Astronomy & Astrophysics* **558**, A33 (Oct. 2013).

[32] Day, C., "LEO Radiation, Its Effects on Electronics and Mitigation Approaches, A Primer," (2009).

[33] Kneller, E., Hyer, K., McIntyre, T., Jones, D., and Swenson, C., "Cadet: A High Data Rate Software Defined Radio for SmallSat Applications," *AIAA/USU Conference on Small Satellites* (Aug. 2012).

[34] Astronautical Development, L., "Li-1 Radio User Manual Revision 0.4," (Sept. 2009).

[35] Bendek, E., Lynch, D., Pluzhnik, E., Belikov, R., Klamm, B., Hyde, E., and Mumm, K., "Development of a miniaturized deformable mirror controller," **9909**, 990984–990984–12 (2016).

[36] Fischer, D. A. and Valenti, J., "The Planet-Metallicity Correlation," *ApJ* **622**(2), 1102 (2005).

[37] Milne, J. S. and Kaufman, D. S., "General Environmental Verification Specification," (Jan. 2003).